

RESEARCH ARTICLE

10.1029/2018JC013793

Special Section:

Sea State and Boundary Layer Physics of the Emerging Arctic Ocean

Key Points:

- Spatial wavefield properties are accurately retrieved from space-borne SAR observations
- Wave height evolution off-ice can be more rapid than in off-land situation
- Wave evolution can be described based on an effective fetch, and accurate ice masks are required

Correspondence to:

J. Gemmrich,
gemmrich@uvic.ca

Citation:

Gemmrich, J., Rogers, W. E., Thomson, J., & Lehner, S. (2018). Wave evolution in off-ice wind conditions. *Journal of Geophysical Research: Oceans*, 123. <https://doi.org/10.1029/2018JC013793>

Received 12 JAN 2018

Accepted 22 JUN 2018

Accepted article online 10 JUL 2018

Wave Evolution in Off-Ice Wind Conditions

Johannes Gemmrich¹, W. Erick Rogers², Jim Thomson³, and Susanne Lehner⁴

¹Department of Physics and Astronomy, University of Victoria, Victoria, British Columbia, Canada, ²Naval Research Laboratory, Stennis Space Center, MS, USA, ³Applied Physics Laboratory, University of Washington, Seattle, WA, USA, ⁴German Aerospace Centre (DLR), Cologne, Germany

Abstract The reduction of the sea ice coverage increases the importance of wind waves in the Arctic. Updates to the standard spectral wave models in recent years have included many aspects of wave-ice interaction. Here we use high-resolution wave parameters retrieved from TerraSAR-X images and in situ SWIFT buoy observations to evaluate the performance of WAVEWATCH III[®] in ice-free waters in the western Arctic over a 7-week period including the fall freeze-up. About two thirds of the analyzed data sets show a good agreement between observations and model results. In other cases, more accurate representation of the wind input fields and the ice coverage could improve the model predictions. Two data sets with larger discrepancy are discussed in more detail. In these two cases of low model skill, with off-ice wind conditions, we show that the model wind-sea growth is too weak to match TerraSAR-X observations, and this situation is improved only slightly by including the effects of atmospheric stability using existing methods. Application of an effective fetch parameterization, which allows for reduced wave generation within the marginal ice zone prior to the open ocean, provides the best estimation of wave growth during off-ice winds.

1. Introduction

The Arctic has been experiencing a continuous reduction of the summer sea ice coverage in the last few decades. The vast areas of open water are susceptible to wave generation. A wind and wave reanalysis in the Beaufort, Bering, and Chukchi Seas for the period 1970 to 2013 shows an increase per decade of about 6% for mean wavelength and 3–8% for significant wave height but no significant increase in wind speed (Wang et al., 2015). Significant wave heights H_s of 1–2 m are now typical for the open waters in the western Arctic (Thomson et al., 2016), and significant wave heights of 4–5 m have been observed in 2012 (Thomson & Rogers, 2014) and in 2015 (see Thomson et al., 2018; this study). These higher sea states and longer wavelengths will likely lead to increased coastal erosion, may affect the breakup of ice sheets, and enhance upper ocean mixing. In turn, wave-induced mixing can release heat from the upper ocean, which can contribute to the melting of sea ice. This effect has been observed in the Beaufort Sea (Smith et al., 2018) and might be the case in the inflow region around Svalbard, where the extension of the North Atlantic Current dips under colder water masses near the surface (as suggested by one of the reviewers).

However, the sea state in the open waters of the Arctic Ocean is currently not monitored on a regular basis. Observations of surface wave properties by commonly used long-term moorings, equipped with surface wave buoys or subsurface acoustic profilers, are impractical in seasonally ice-covered waters. Remote sensing methods can provide a viable alternative to in situ wave observation in the Arctic (Gemmrich et al., 2015; Gebhardt et al., 2017).

Under the idealized case of a steady wind blowing perpendicular to an infinite straight shore, wave parameters for different wind speeds and fetches can be expressed in terms of a single nondimensional fetch parameter

$$\tilde{X} = gXu^{-2}, \tag{1}$$

where g is the acceleration due to gravity, u is the wind speed, usually observed at 10-m height, and X is the distance to the shore. Then the evolution of the wave spectra follows a similarity law that leads to a power

law scaling of the nondimensional dominant wave period $\tilde{T} = gT/u$ and the nondimensional significant wave height $\tilde{H}_s = gH_s u^{-2}$:

$$\tilde{T} = a_1 \tilde{X}^{b_1}, \quad (2)$$

$$\tilde{H}_s = a_2 \tilde{X}^{b_2}. \quad (3)$$

As an alternative to \tilde{H}_s , the nondimensional wave energy $\tilde{\epsilon} = \epsilon g^2 / u^4$ is commonly used, where $\epsilon = \langle \eta^2 \rangle$ is the variance of the surface elevation η .

Several wave growth experiments were performed in the 1970s and 1980s, starting with the classic Joint North Sea Wave Project (JONSWAP) experiment (Hasselmann et al., 1973). These experiments showed reasonable agreement with the power law scaling but significant scatter between the various data sets. Kahma and Calkoen (1992, KC92 hereinafter) reconciled these discrepancies by considering atmospheric stratification and correcting for unsteady wind conditions. Thus, JONSWAP and KC92 are now widely accepted scaling for fetch-limited wave growth (Holthuijsen, 2007). However, it is not established how well these scalings perform in conditions of wind blowing off ice, especially over a wide marginal ice zone (MIZ), where wave generation is likely to occur in the ice-infested water. Here the TerraSAR-X observations provide a unique opportunity to evaluate wave evolution with a very high fetch resolution.

Recently, Smith and Thomson (2016) evaluated the fetch dependence of waves in the western Arctic and in particular the dependence in partial ice cover. They found that waves in open water are fetch-limited about one fourth of the time during the summer months (with the other cases being either duration limited or unsteady). They found that waves in partial ice cover also can be fetch limited, if they are associated with off-ice winds. Off-ice winds generate waves locally within the partial ice cover, as opposed to cases with remotely generated waves propagating into an ice field. The local generation of waves is less effective in partial ice cover than it is in open water, and this can be accounted for in the conventional fetch laws by using an effective fetch that is less than the actual fetch. The effective fetch adjustment is shown, empirically, to be a function of ice concentration. The general conclusion of Smith and Thomson (2016) is that ice cover is a dominant feature in controlling wave generation in the western Arctic, both in the regional sense of limiting the open water fetch and in the local sense of slowing the growth of waves within partial ice cover.

2. Wave Parameter Retrieval From TerraSAR-X

Over the ocean, synthetic aperture radar (SAR) is capable of providing wind and wave information by measuring the roughness of the sea surface. TerraSAR-X provides high-resolution imagery that is particularly suited to investigate small-scale changes of sea surface roughness. Modes and processing of the TerraSAR imagery is described in Breit et al. (2010). TerraSAR-X data have been used to investigate the highly variable wave climate in coastal areas (Bruck & Lehner, 2013) and the open ocean (Gemrich et al., 2016). In addition, accurate estimates of the wind field over the ocean are obtained from TerraSAR-X data.

TerraSAR-X operates in the X-band with 31-mm wavelength from 15 Sun-synchronous orbits per day at 514 km, yielding a repeat cycle of 11 days. However, by varying the SAR incidence angle, repeat coverage in polar regions can be achieved, usually at least with one of the daily ascending or descending satellite paths, often with both. The TerraSAR-X data used for this study are Multilook Ground Range Detected standard products. We use VV polarization in the so-called stripmap mode, which covers a 30-km-wide swath at a pixel spacing of 2.5 m. Image intensity is converted to normalized radar cross section σ_0 (Pleskachevsky et al., 2016), which is the basis for the retrieval of wind speed u , significant wave height H_s , wavelength λ , and wave direction d_w (Gemrich et al., 2016).

The retrieval of wind speeds from TerraSAR-X data is based on the XMOD algorithm (Ren et al., 2012). The normalized radar cross section σ_0 is a function of the incidence angle α , the wind direction ϕ relative to the SAR flight direction, and the wind speed U .

$$\sigma_0 = a_0 + a_1 U + a_2 \sin(\alpha) + (a_3 + a_4 U) \cos(2\phi), \quad (4)$$

where $a_0 \dots a_4$ are empirical constants and σ_0 is given in decibel. The wind speed U is calculated solving (4) iteratively.

The retrieval of the wave parameters H_s , λ_p , and d_w is all based on the 2-D Fourier transform of the SAR image. Similar to the the open ocean, the H_s retrieval is obtained with the modified empirical X-WAVE model function (Gemrich et al., 2016; Rikka et al., 2018).

$$H_s = C_0(\beta) + C_1 \sqrt{E \tan(\alpha)} + C_2 E_{ice}, \quad (5)$$

where C_0 , C_1 , and C_2 are empirical coefficients and β is the angle between the dominant wave direction and the satellite flight direction. The parameter E is a measure of the integral power P of the scaled radar backscatter

$$\tilde{\sigma} = \frac{\sigma_o}{\bar{\sigma}_o} - 1 : \quad (6)$$

$$E = \int_{k_1}^{k_2} \int_0^{2\pi} P(k, \theta) dk d\theta, \quad (7)$$

truncated to wave numbers k_1 to k_2 corresponding to wavelengths between 500 and 30 m. The first two terms of (5) are the same as for the open ocean condition. The empirical coefficients are tuned to include the energy of the unresolved high wave number scales. In the Arctic, even weak ice infestation can dominate the 2-D image spectrum. Therefore, we modify the open ocean algorithm to account for small wave number energy associated with ice floes: $C_2 E_{ice}$, where $C_2 < 0$ and E_{ice} are scaled integral measures of the power at wave numbers $< 0.9k_p$, with dominant wave number k_p .

3. Wave Model

The WAVEWATCH III® model (The WAVEWATCH III Development Group [WW3DG], 2016) is applied in a hind-cast. Open water physics are represented with the Ardhuin et al. (2010) parameterizations (denoted *ST4*) with $\beta_{max} = 1.2$. The latter is a parameter in *ST4* to accommodate gross wind bias. Thermal stability effects are included via the parameterization known as *STAB3* in *WW3* (Abdalla & Bidlot, 2001). Air-sea temperature differences are taken from the Navy Global Atmospheric Model analyses. The wind input source function is scaled by open water fraction (see *WW3DG*, 2016; Rogers et al., 2016). The grid used is the 5 km (irregular) inner grid used in section 4 of Collins and Rogers (2017). Run time is 0000 UTC 2 September 2015 to 0000 UTC 10 November 2015 with a cold start. The IC4M6 parametric/empirical representation of wave attenuation by sea ice S_{ice} is used (Collins & Rogers, 2017), though it is noted that the choice of S_{ice} parameterization has reduced relevance in cases of off-ice winds: rather, the open water source terms and input fields (winds and ice) are of primary importance. This model was forced with winds from the Navy Global Atmospheric Model (Hogan et al., 2014) with nominal 0.28° resolution. Ice concentration comes from Advanced Microwave Scanning Radiometer 2 (AMSR2) of the Japanese Space Agency, JAXA. These fields are created from swath data as described in Collins and Rogers (2017), but here the ice concentration values were computed using the *bootstrap* algorithm (Comiso et al., 2003). The data were processed from microwave brightness temperatures by Dr. Li Li of the Naval Research Laboratory. These Bootstrap fields are evaluated in the context of similar cases in Rogers et al. (2018). The algorithm uses the 18-, 37-, and 89-GHz channels of AMSR2. Geographic resolution is 10 km, and mean temporal resolution (interval between swaths) is 5.3 hr. *WW3* interpolates wind fields in the time domain, but for the ice concentration fields it simply uses nearest field in time.

4. Significant Wave Height

4.1. SAR Data Versus Wave Model

TerraSAR-X stripmap images of various swath length have been obtained in the Beaufort Sea between 7 September and 3 November 2015 in support of the R/V Sikuliaq cruise (Thomson et al., 2018). A total of 17 of these images includes sections that are ice-free adjacent to the MIZ and are suitable for the extraction of wavefield parameters. In particular, the significant wave height H_s is retrieved for each image subsection of $2,048 \times 2,048$ pixels, that is, $5,120 \text{ m} \times 5,120 \text{ m}$, yielding 438 observations. Here ice free is defined as subscenes where the *WW3* ice mask shows values of ice concentration < 0.1 . Corresponding H_s values are extracted from the *WW3* model runs by linear 2-D interpolation from the coarser model grid to the center of the TerraSAR-X subscenes and times closest to the SAR acquisition time. Thus, the observations and model times can differ by up to ± 1.5 hr. In about two thirds of the cases, the predicted H_s is in good agreement with the observations (Figure 1). Taking all 438 observation-model pairs as a single population for calculating statistics, the overall normalized bias is 0.16, and the overall scatter index is 0.36. However, the quality of the model predictions varies widely between the individual data sets, for example, for individual data sets the bias ranges from -0.34

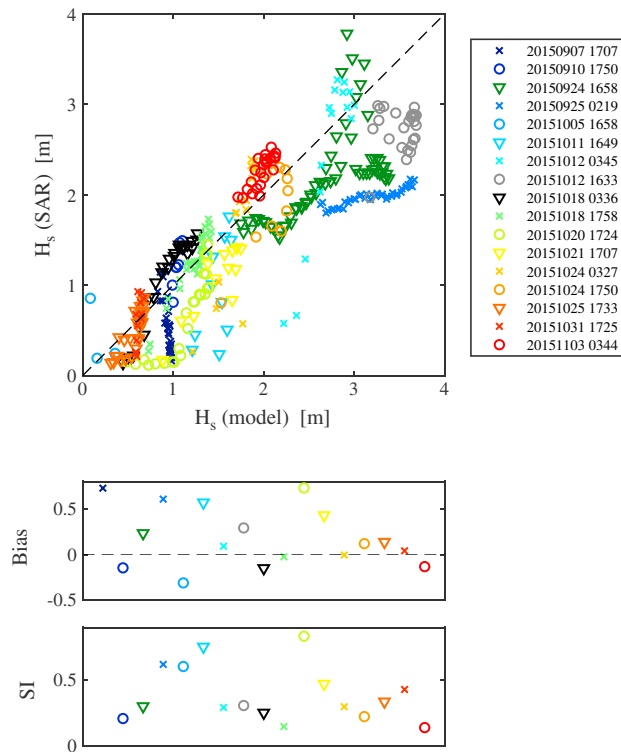


Figure 1. Comparison of significant wave height obtained from the TerraSAR-X images, H_s (SAR), and from the wave model, H_s (model), for all data sets (top) and associated normalized bias (middle) and scatter index (SI) (bottom). SAR = synthetic aperture radar.

to 0.69, with the smallest absolute value of the normalized bias of 0.005, and a median of 0.089. Similarly, the scatter index spans a range of 0.09 to 0.88, with the median of 0.27 (Figure 1).

Factors causing significant wave model bias and large scatter indices can be numerous. The most common causes are incorrect input wind fields, unresolved bathymetry, and incorrectly represented or missing physical processes, where the wind field uncertainties are likely the dominant cause. In the data set at hand, the difference in H_s between the model and observations $\Delta H_s = H_s(\text{model}) - H_s(\text{SAR})$ cannot be attributed solely to differences in the wind field $\Delta u = u(\text{model}) - u(\text{SAR})$. In about two thirds of the individual data, larger (smaller) model wave heights are associated with higher (lower) model wind speeds (Figure 2). For nine individual data

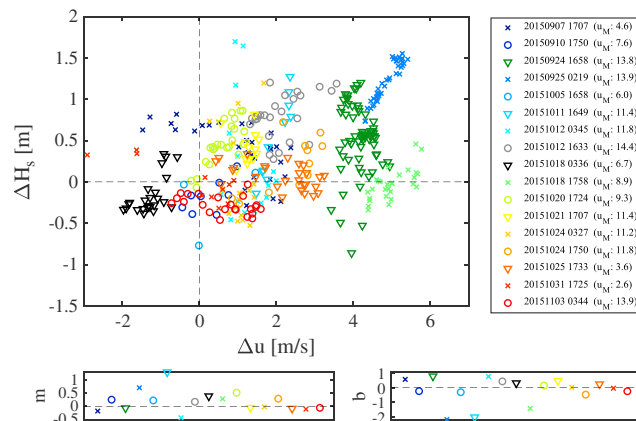


Figure 2. (Top) Difference of significant wave height ΔH_s as function of difference in wind speed Δu_{10} , where the differences are taken between model results and values retrieved from the synthetic aperture radar images. The observation times and mean model wind speeds u_M (in meter per second) are given in the legend. (Bottom) Slope m and axis intercept b of linear fit $\Delta H_s = m \Delta u + b$, for data sets with statistically significant correlations.

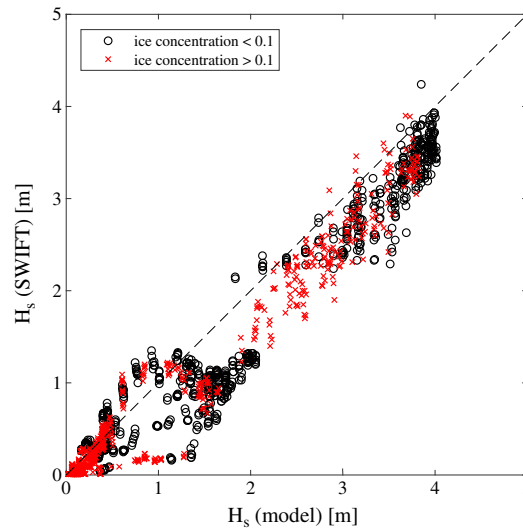


Figure 3. Comparison of significant wave height obtained from the SWIFT in situ observations, $H_s(\text{SWIFT})$, and from the wave model, $H_s(\text{model})$, for all SWIFT data sets.

sets, there is a positive correlation, significant at the 95% level, between ΔH_s and Δu . In two data sets the correlation is negative and significant, and in six cases there is no significant correlation (Figure 2). In the cases 25 September and 12 October, 16:33, the large model bias is likely due to the large wind speed discrepancy. However, there is no consistent relationship between Δu and ΔH_s , even for the cases where wind speed anomaly and wave height anomaly are positively correlated, in particular the fitted value $b = \Delta H_s(\Delta u = 0)$ varies widely (Figure 2), and other factors than wind speed discrepancies must play a role, too. In the Arctic, wave generation, propagation, and dissipation are strongly affected by the presence of ice. Thus, uncertainties in the ice coverage and ice type and incomplete wave-ice physics can have a major impact on the predicted wave heights. These effects are likely the reason for the large bias on 24 September, where the SAR image shows the remnants of an ice tongue, which is much weaker in the model and does not reach the SAR image region. Uncertainties of the location of the ice edge of a few tens of kilometers can have a significant impact (3 November), as well as incomplete representation of the physics of the polar atmospheric boundary layer (10 September). These cases will be discussed in more detail in section 5.

4.2. SWIFT Data Versus Wave Model

In situ wave observations were obtained with a set of SWIFT buoys (Thomson, 2012) as well as a ship-mounted laser gauge. The main overall focus of the experiment was the study of atmosphere and ocean boundary layer processes related to the MIZ. Therefore, ship observations in the open water were limited. Furthermore, positioning of the freely drifting SWIFT buoys within the 30-km-wide TerraSAR-X stripmap image proved to be difficult in this cruise with multiple objectives. Therefore, there are no coinciding open water in situ wave observations and SAR observations in this data set. However, previous experiments in the open ocean (Gemrich et al., 2016) and limited data in the ice-free Arctic (Gemrich et al., 2015) showed good agreement between H_s values retrieved from TerraSAR-X data and SWIFT observations. An evaluation of the model results against the SWIFT observations can provide an indirect assessment of the comparison of the model and the SAR-retrieved H_s data, given in Figure 1. About 1,500 H_s values were obtained with the SWIFT buoys during the R/V Sikuliaq cruise. We extract the corresponding model H_s and ice concentration values based on 2-D interpolation (Figure 3). The time uncertainty is ± 1.5 hr, the same as in the comparison with the SAR-data. The SWIFT buoys operated in open water as well as the MIZ. About 48% of the data are at locations where the model based ice-concentration is < 0.1 , similar to the conditions of the SAR H_s retrievals. The comparison between the model and the SWIFT buoys have very similar statistics as the SAR-model comparison: the scatter index is 0.28 (0.39) and the normalized bias 0.21 (0.23) for locations with ice concentration > 0.1 (< 0.1). Thus, for the evaluation of the model performance, the SAR-retrieved wave heights and buoy data are similarly well suited.

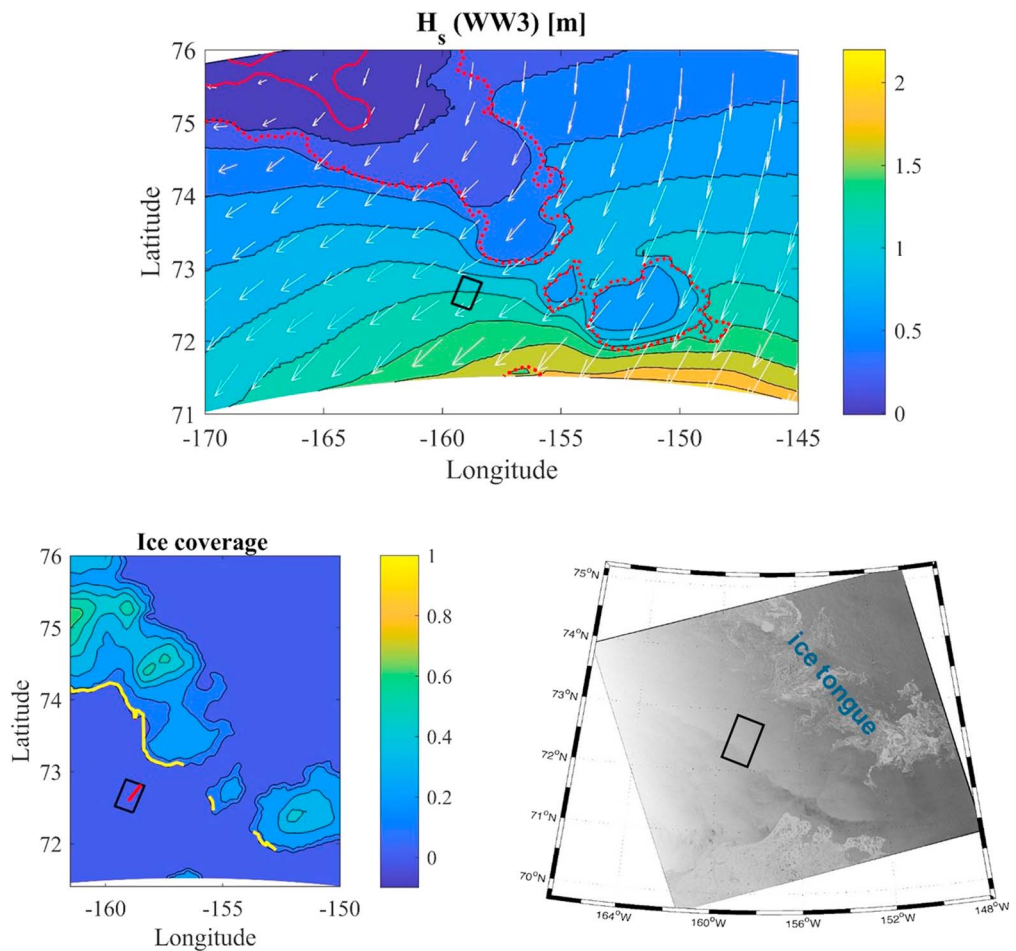


Figure 4. Model results for 10 September 2015, 18:00. The area of the TerraSAR-X-image is indicated by the black rectangle. (Top) Significant wave height H_s (m), wind vectors (normalized), and ice concentration (dots: 0.1, line: 0.9). (Bottom left) Ice concentration. The yellow line indicates the 10% ice contour taken as fetch = 0, and the red arrow gives the direction of wave propagation. (Bottom right) RADARSAT-2 image (MacDonald, Dettwiler, and Associates Ltd., All Rights Reserved). WW3 = WAVEWATCH III.

5. Evolution of Wave Parameters in Off-Ice Wind Condition

In about half of our data sets the discrepancy between model H_s and SAR observations can be attributed to a large extent to differences in the wind speed. In the following we discuss two cases where uncertainties in the ice coverage and incomplete representation of the physics are likely the reason for the anomalies in the wave model results. Both cases contain the evolution of the wavefield in off-ice wind conditions.

5.1. Diffuse MIZ

The first case of off-ice wind condition discussed here occurred on 10 September and thus during the pre-cruise phase of the SeaState project (Thomson et al, 2018). A short TerraSAR-X stripmap is located roughly 110 km to the southeast of the remnants of an ice tongue (Figure 4). This ice tongue was generated by the partial melt of the ice in the Canada Basin in mid-August and persisted until the end of September. The wind direction was from northeast; that is, the SAR image is downwind from a diffuse ice-covered area. The average wind speed over the image region is 7.5 m/s, and the significant wave height varies between 0.7 and 1.8 m (Figures 1 and 5).

The ice mask in the model shows the ice tongue as several broken-up ice patches with maximum ice concentration ≤ 0.5 upwind from the SAR image (Figure 4). As a consequence, the model prediction shows only a small reduction in H_s within the ice tongue and only a very weak effect of the ice tongue on H_s values in the area of the SAR image (Figure 4). Thus, in the model the wavefield in the region of the SAR image is not fetch

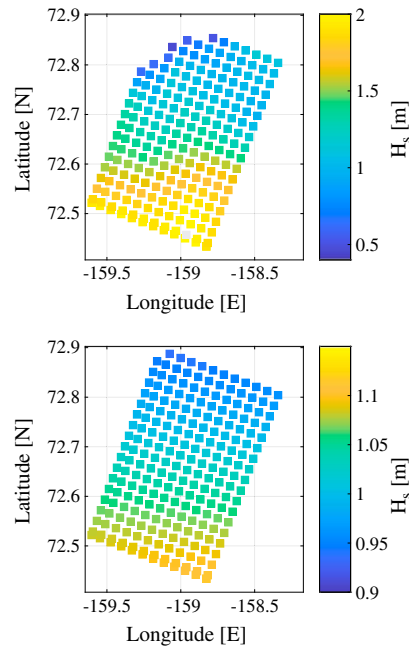


Figure 5. Spatial field of significant wave height H_s , retrieved from TerraSAR-X image from 10 September 2015, 1750 UTC (top) and corresponding WAVEWATCH III model results, interpolated onto same grid points as the TerraSAR-X results (bottom). (Note the different ranges in H_s .)

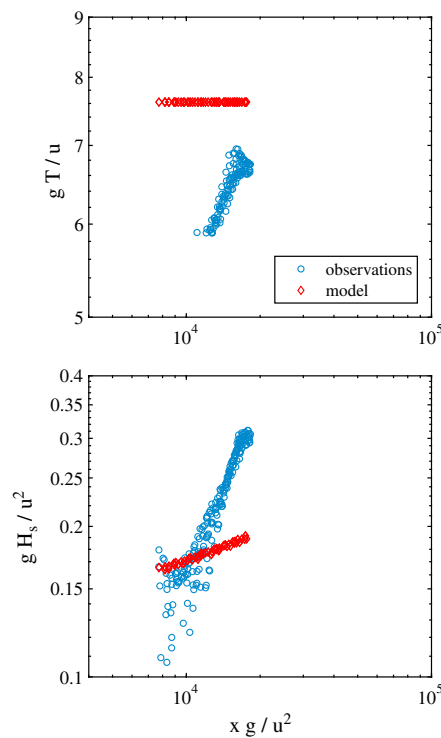


Figure 6. Fetch evolution of wavefield obtained from synthetic aperture radar image on 10 September 2015, 17:50. (Top) Nondimensional wave period as function of nondimensional fetch. (Bottom) Nondimensional wave height as function of nondimensional fetch.

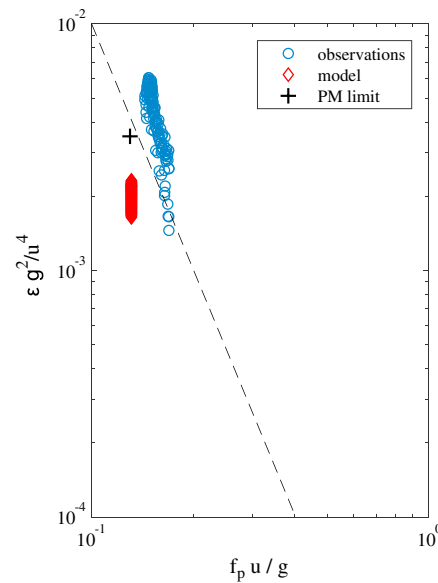


Figure 7. Wave growth similarity scaling: nondimensional wave energy as function of nondimensional wave frequency for 10 September 2015, 17:50. The dashed line represents a power law with exponent $-10/3$. The black cross indicates the asymptotic limit of wave evolution given by the Pierson-Moskowitz (PM) spectrum.

limited by the ice tongue, and the model H_s increases slowly from about 0.9 to 1.1 m (Figure 5), and the peak wave period remains constant at $T_p = 5.9$ s.

In contrast to the model results, the SAR observations reveal a very significant evolution of the wavefield. The significant wave height increases from about 0.9 to 1.9 m over the roughly 50-km length of the TerraSAR-X swath (Figure 5). Close to the northern edge of the SAR image, the wavelengths are shorter than the cut-off for the given SAR image mode (30 m). However, within the bulk of the image, the dominant wavelength increases to 45 m, corresponding to a dominant wave period $T_p = 5.3$ s (not shown). Thus, the model indicates a wavefield evolution consistent with a fetch on a scale of hundreds of kilometers, whereas the SAR-retrieved wavefield indicates a fetch of tens of kilometers.

The different rates of wave evolution can also be seen in the nondimensional plots of wave period or wave height as function of fetch (Figure 6). Here we calculate fetch as distance from the downwind edge of the ice tongue (yellow line in Figure 4). The SAR-retrieved data show a rapid increase of wave height and wave period (or wavelength) with increasing fetch, and the data collapse onto a power law. The wave height evolution in the model also collapses onto a single line, but with a much smaller slope, which suggests wind forcing that is much too weak, even though the model wind speed ($u_{10} = 7$ to 7.5 m/s) is not much less than the observed wind speed ($u_{10} = 7.5$ m/s). Again, at the given resolution of the wave period values stay constant over the short distance of the SAR image. The classic scaling laws of KC92 or JONSWAP are not applicable because the wave energy within the ice field does not drop to negligible values in the wave model and likely also in the observations. Therefore, the waves within the SAR area do not represent a conventional fetch evolution, at least not in the model results. Because the wave growth associated with the winds from the east-northeast is so weak, the model wave conditions are in fact dominated by a swell from the northwest at the TerraSAR-X locations. Thus, it is not expected that the wave height and peak period would exhibit any simple fetch relation with those winds.

The similarity scaling of the wave evolution predicts a power law scaling of the nondimensional energy and the nondimensional frequency

$$\tilde{\epsilon} \propto \tilde{f}_p^n, \tag{8}$$

where $\tilde{f}_p = f_p u g^{-1}$. Badulin et al. (2007) argue that self-similar wave growth scales by internal wave-field properties such as the fluxes of energy, momentum, or wave action. For young waves and constant momentum flux the exponent $n = -10/3$, and for well-developed waves, where the energetic part of wave spectrum

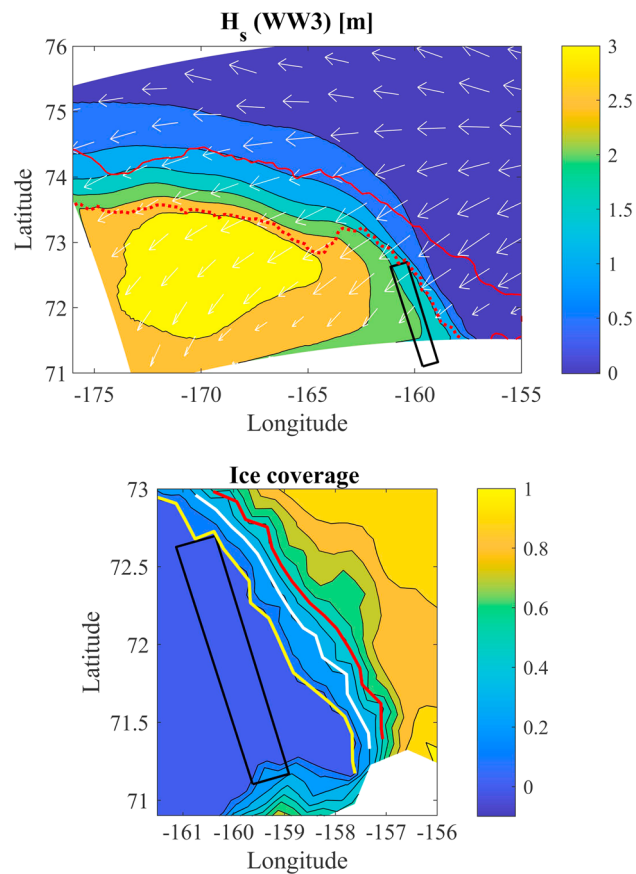


Figure 8. Model results for 3 November 2015, 03:00. The area of the TerraSAR-X-image is indicated by the black rectangle. (Top) Significant wave height H_s (m), wind vectors (normalized), and ice concentration (dots: 0.1, line: 0.9). (Bottom) Ice concentration. The yellow, white, and red lines indicate three choices for fetch = 0. WW3 = WAVEWATCH III.

is driven by nonlinear wave interactions rather than by the wind, $n = -8/3$. The limiting values for the Pierson-Moskowitz spectrum are $\tilde{f}_p = 0.13$ and $\tilde{\epsilon} = 3.5 \times 10^{-3}$. The rapid wave evolution observed in the SAR-retrieved data is consistent with the self similarity scaling (8) for young seas, $n = -10/3$ (Figure 7). However, the energy levels are about twice as high as expected under regular, ice-free conditions. On the other hand, the model results show much lower energy levels than the Pierson-Moskowitz level, suggesting that the ice tongue attenuated the wave energy without affecting the peak wave frequency. The power law behavior of the model wave evolution cannot be evaluated, since the model wave period is associated with swell from the northwest and remains constant within the SAR area.

5.2. Narrow MIZ

A TerraSAR-X stripmap was acquired on 3 November 2015 at 03:44 over the eastern Chukchi Sea. This followed a rapid freeze-up of the Beaufort Sea in the previous days, yielding full ice coverage to the east and north of the stripmap location (Figure 8). A strong off-ice wind event with average wind speeds $u = 13.5$ m/s and wind direction from east-northeast generated an evolving wavefield that reached maximum H_s values of >2.5 m in the center of the Chukchi Sea, about 250 km from the ice edge. The orientation of the TerraSAR-X image is at a small angle to the ice edge, yielding dimensional fetches of approximately $10 \text{ km} < X < 100 \text{ km}$ for the individual image subscenes. In the classical case of wave-fetch evolution off land the start of the fetch, $X = 0$, is simply the coast. In a wide MIZ, some wave generation is likely to occur in ice-infested water. Therefore, it is not immediately obvious what corresponds to $X = 0$ in the case of off-MIZ wind. As a low estimate, we pick the ice concentration = 0.1 contour line (Figure 8, yellow line). A more conservative estimate where the fetch origin is at ice concentration 0.5 (Figure 8, red line) gives on average an increase in dimensional fetch of 35 km. Additionally, we examine the fetch evolution if ice concentration 0.3 is taken as the origin (Figure 8, white line). In the following, these choices of fetch origin are labeled FC01, FC03, and FC05.

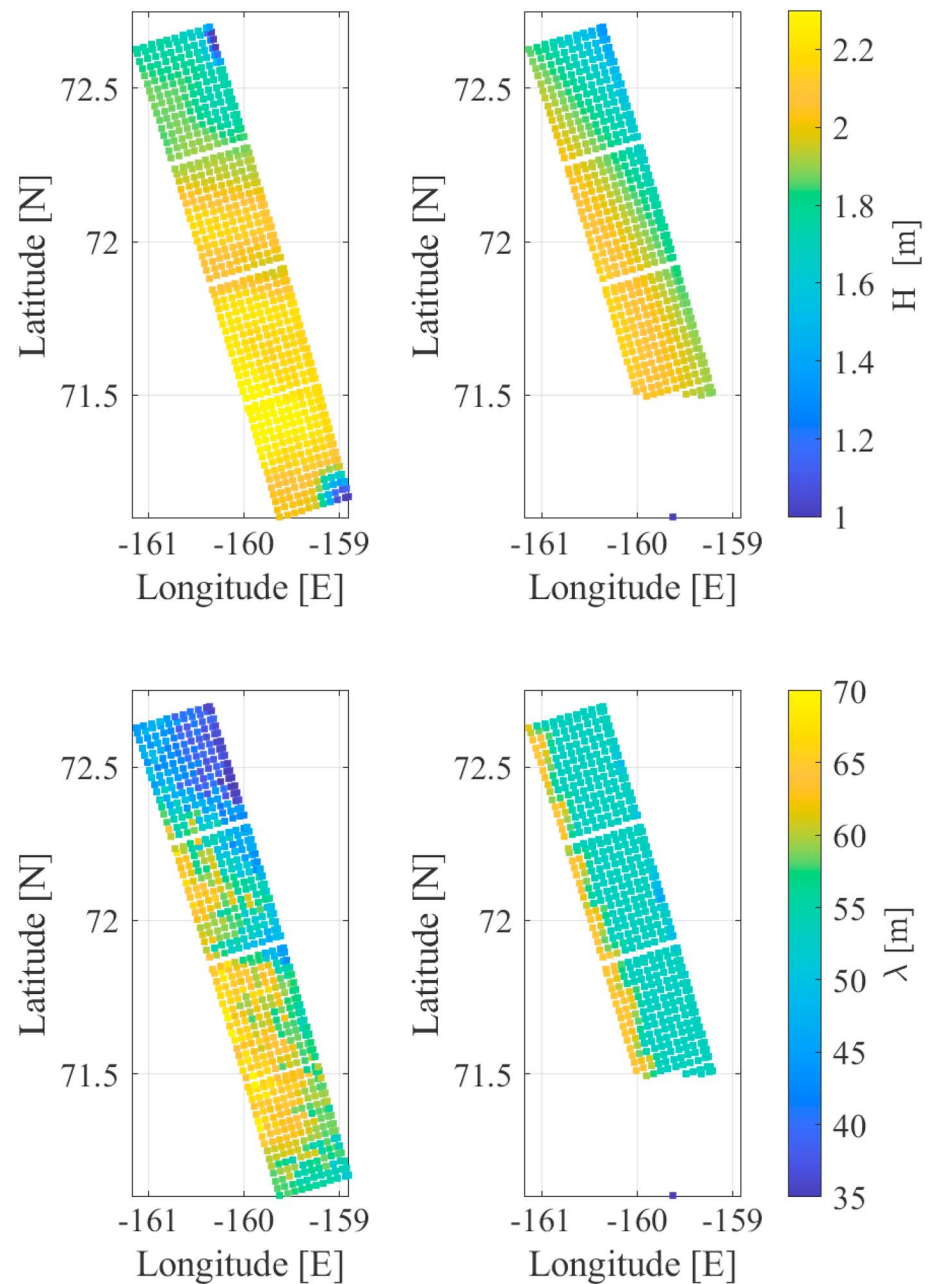


Figure 9. Spatial field of significant wave height H_s (top) and dominant wavelength (bottom) for 3 November 2015. (Left column) Values retrieved from TerraSAR-X image at 03:54. (Right column) values from WAVEWATCH III model at 03:00, interpolated onto same grid points as the TerraSAR-X results.

Wave height and dominant wave period increase with increasing fetch, both in the SAR observations and the model (Figure 9). The observed and modeled wave evolution is consistent with the wind direction 80° as obtained from the model and retrieved from the SAR image. However, the dominant wave direction in the model is 115° , that is, waves coming from east-southeast. This results in slightly longer fetches in the northwest corner of the SAR image than fetches based on the wind direction.

To compare the data with existing similarity laws of fetch-limited wave evolution, the data are nondimensionalized based on the mean model wind speed in the SAR area $u = \bar{u}(\text{model}) = 13.5\text{m/s}$, which is slightly higher than the mean wind speed retrieved from the SAR image, $\bar{u}(\text{SAR}) = 13.2\text{m/s}$. For the model results, the distance to the fetch origin is calculated in direction of the wave propagation and for the SAR data based

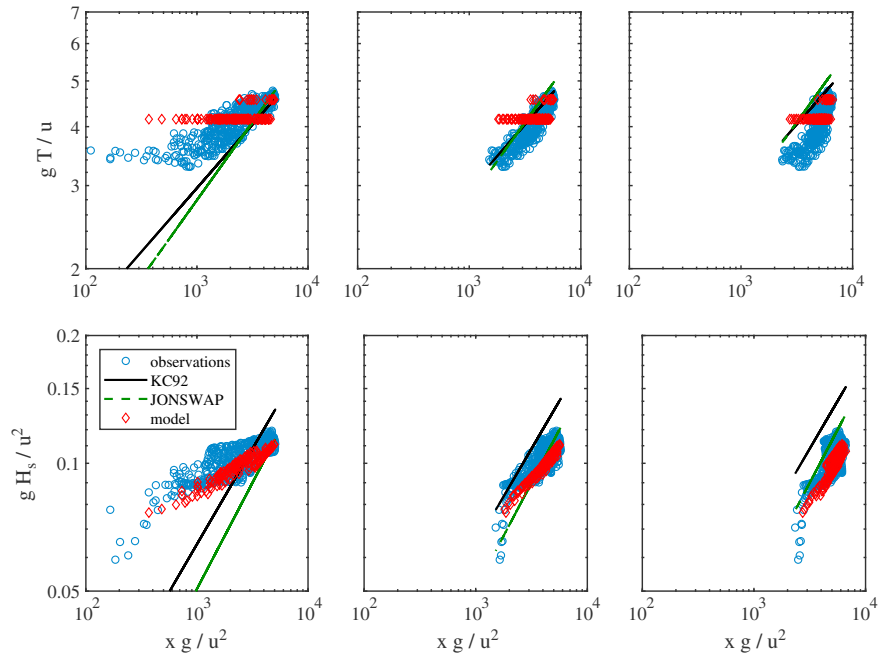


Figure 10. Fetch evolution obtained from synthetic aperture radar image on 3 November 2015, 03:34, and WAVEWATCH III model for 3 November 2015, 03:00. (Top row) Nondimensional wave period. (Bottom row) Nondimensional wave height. Columns represent different fetch origins. (Left) For fetch starting at ice concentration 0.1 (yellow line in Figure 8); (middle) at ice concentration 0.3 (white line), and (right) at ice concentration 0.5 (red line). Lines indicate the results from Joint North Sea Wave Project (JONSWAP) and Kahma and Calhoun (1992, KC92).

on the wind direction. The SAR-retrieved wavelength is converted to wave period based on the deep water dispersion relation (Figure 10).

For FC01, the observed dominant wave period is longer and less rapid than the scalings of JONSWAP or KC92 predict (Figure 10, left). A relative small increase in fetch, FC03, brings the observations in reasonable agreement with the classical scalings; however, the evolution of the wave height is slower than in the parametric models. The scatter of the data is too large to determine whether JONSWAP or KC92 is a better fit (Figure 10, middle). In the case of the fetch origin at 50% ice coverage, FC05, the observed wave periods are smaller than the scaling laws predict, but the evolution of the wave height is in good agreement with JONSWAP (Figure 10, right). The model wave period is less dynamic than the observed values and clearly shows the limitations of the model frequency resolution.

The fetch evolution of the wave period suggests a fetch origin at the 30% ice contour, whereas the evolution of the wave energy is more consistent with a fetch origin at 50% ice coverage. Taking the fetch origin even further into the MIZ would not improve the fit with the existing scaling laws.

Setting the fetch origin at a somewhat arbitrary ice contour effectively assumes open-water wave growth at the region of lower ice coverage and zero wave evolution in the region with ice coverage higher than the chosen contour. As seen in Figure 10, this can lead to results in reasonable agreement with the existing scaling laws. However, this approach is not satisfying from a physics point of view. A more appealing concept is a *cumulative* fetch, where the wave growth occurs throughout the entire MIZ, but with its effectiveness reduced in higher ice coverage.

$$X_c = \alpha \sum X_i (1 - \gamma_i)^m, \quad (9)$$

where X_i is the downwind width of the region with ice fraction γ_i , and α is a weighting factor with $0 < \alpha \leq 1$. We find good agreement of the SAR-retrieved wave evolution and the parametric scaling laws for $m = 1$ and $\alpha = 0.8$ (Figure 11). The model wave heights show the same rate of wave growths, but offset to larger fetches compared to JONSWAP or KC92. We tested different combinations of values for m and α and find a linear scaling and a weight factor $\alpha = 0.8$ give the best fit with simple physical explanation: The wave growth in partial ice covered regions is effectively 80% of the wave growth in the ice-free fraction of that region.

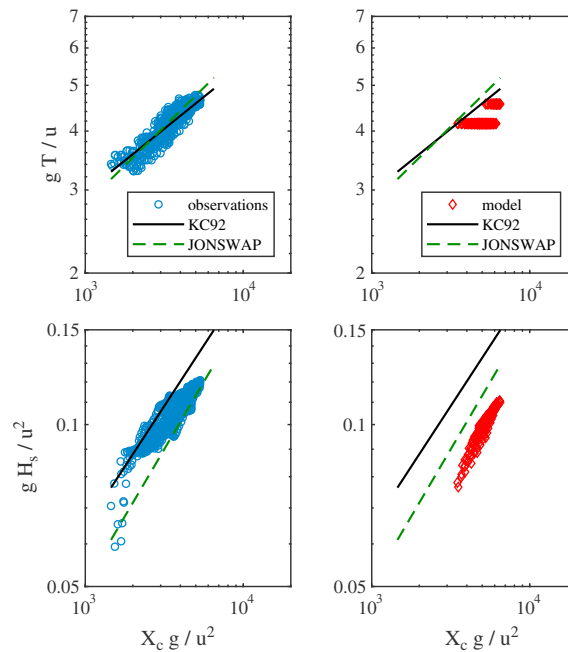


Figure 11. Fetch evolution for 3 November 2015 based on a cumulative fetch within the marginal ice zone. (Left column) Results obtained from the synthetic aperture radar image, and (right column) results obtained from the wave model. (Top row) Nondimensional wave period and (bottom row) nondimensional wave height. Lines indicate the results from Joint North Sea Wave Project (JONSWAP) and Kahma and Calhoun (1992, KC92) .

The reduction in wave growth rate, $\alpha < 1$, is consistent with the recent study of Zippel and Thomson (2016), who apply an existing model for the wind input rate to the wavefield that is itself dependent on the energy in the wavefield. Thus, if there is less wave energy present because of partial ice coverage, there will be less wave growth. Zippel and Thomson (2016) apply this feedback mechanism in determining the reductions to the surface flux of turbulence in the MIZ. They suggest that any amount of wave damping or sheltering provided by sea ice will reduce the effectiveness of a given wind stress to grow waves and to create turbulence.

6. Discussion

6.1. Fetch Evolution

In both data sets the fetch evolution of the dominant wave period, i.e., the peak of the wave spectrum, is in good agreement with the scaling in coastal water under strong stratification (KC92). However, the evolution of the significant wave height, i.e., the integrated wave spectrum, is inconsistent with the scaling laws. On 3 November, the observed wave height evolution is slower than suggested by the scaling laws. The choice of the start of wave generation, i.e., zero fetch, has a noticeable impact on the observed scaling of the wave evolution. Clearly, wave generation and growth occurs within the MIZ and fetch evolution based on the outer ice edge underestimates the wave evolution. A more physical approach is the cumulative fetch (9), i.e., the ice-free portion of a region allows for wave evolution but at a reduced rate α . Including this scaled wave growths of the entire MIZ brings the scaling in close agreement with JONSWAP, whereas the exclusion of this region results in wave heights at short fetches that are greater than JONSWAP and KC92 scalings. Here, we find $\alpha = 0.8$. However, the effectiveness of the wave growth within the MIZ is likely a function of the ice type and floe sizes. For example, the dampening of short-scale waves in grease ice likely leads to a weak wave generation, $\alpha \ll 1$, whereas the wave growth in pancake ice or small ice floes is expected to be more effective, $\alpha \lesssim 1$.

In the 10 September case, smaller than expected wave heights are observed at short fetch, and the wave height evolution is more rapid than the scaling laws predict. Our first hypothesis for this rapid wave growth was a seeding of the wavefield within the ice-covered region. However, idealized model runs with different seeds showed that seeding energy at low wavenumbers has only a minor effect on the fetch evolution of H_s that cannot explain the observed rapid fetch evolution. A likely factor contributing to a modified fetch

evolution is an unsteady or nonhomogeneous wind field. Unfortunately, the wind field information at hand does not resolve these issues.

6.2. Accuracy of Ice Forcing

As noted above, high temporal resolution AMSR2 Bootstrap fields were used for the WW3 hindcast. This is, overall, the best ice concentration forcing that we have tested for WW3 but is not universally superior. For the September period, the Global Ocean Forecast System (Metzger et al., 2017; Posey et al., 2015) provides a better representation of the ice tongue, but this system is less accurate during the October period (see Rogers et al., 2016, 2018).

6.3. Experiments With Thermal Stability and Fetch Offset

Off-ice winds tend to be colder than the water underneath, resulting in unstable atmospheric conditions. This will tend to be gustier than stable conditions and result in faster wave growth (Cavaleri, 2000). Thus, it is reasonable to speculate that the model's underprediction of the wave growth for the 10 September case is a result of ignoring atmospheric stability effects in the wave model hindcast.

We first investigated this by determining the *effective wind speed*, which would be required to provide a match between the growth curves, determined using idealized one-dimensional experiments, and the TerraSAR-X growth curves for the 10 September case. It was found that no wind speed provides a good match. However, if the fetch is offset by adding an additional 40 km of fetch to WW3 (or equivalently subtracting this from the TerraSAR-X curves) and with $u_{10} = 10.5$ m/s, agreement between the measurements and the idealized WW3 is excellent. We determined that using the empirical stability algorithm of Tolman (2002; STAB2 in WW3) or that of Abdalla and Bidlot (2001; STAB3 in WW3), no realistic air-sea temperature difference gives an increase in the effective wind speed of $u_{10} = 10.5$ m/s given the actual estimated wind speed of 8.4 m/s.

As noted above, the hindcast includes thermal stability effect by ingesting air-sea temperature differences and activating the STAB3 setting (Abdalla & Bidlot, 2001). As expected, based on the idealized cases, the thermal stability did not produce a large enough increase in the WW3 growth rate, required for better match to TerraSAR-X retrieved wavefields for the two cases studied in detail here.

7. Conclusion

The hugely increased seasonal retreat of ice coverage has opened the Arctic for significant wave generation. From a wave model point of view, the Arctic has become a marginal sea. However, the presence of ice does not only affect the wave prediction in the MIZ or the fully ice-covered region. Even in the ice-free section, the evolution of the wavefield can be affected by the ice for distances of tens to hundred kilometers from the ice edge. The wave models include processes to represent this, but some of the details, such as the scaling of wind input by open water fraction, are ad hoc and unverified. Parameterizations for thermal stability effects also require scrutiny, since this process may play a role in the observed strong growth in the two cases studied here, where the model performs poorly. A detailed ice mask is crucial for accurate wave predictions near the ice edge. We have shown that in the MIZ, the wave evolution can be described by a cumulative fetch evolution, where the fetch is weighted by the ice fraction in a variable ice coverage. Satellite-based SAR observations are uniquely suited for process studies that involve wave and ice observations in the Arctic and provide a high resolution spatial coverage that is very rarely achieved with in situ observations. On longer time scales, global altimeter and SAR wave mode data will be well suited for validation of wave models of the Arctic and could as well be used for assimilation.

References

- Abdalla, S., & Bidlot, J. R. (2001). Wind gustiness and air density effects and other key changes to wave model in CY25R1 (Tech. Rep. memorandum r60.9/sa/0273, Tech. Rep.). U. K.: ECMWF, Reading, Research Department.
- Ardhuin, F., Rogers, W. E., Babanin, A., Filipot, J.-F., Magne, R., Roland, A., et al. (2010). Semi-empirical dissipation source functions for ocean waves. Part I: Definitions, calibration and validations. *Journal of Physical Oceanography*, *40*, 1917–1941.
- Badulin, S., Babanin, A., Zakharov, V. E., & Resio, D. (2007). Weakly turbulent laws of wind-wave growth. *Journal of Fluid Mechanics*, *591*, 339–378. <https://doi.org/10.1017/S0022112007008282>
- Breit, H., Fritz, T., Balss, U., Lachaise, M., Niedermeier, A., & Vonavka, M. (2010). TerraSAR-X SAR processing and products. *IEEE Transactions on Geoscience and Remote Sensing*, *48*, 727–740.
- Bruck, M., & Lehner, S. (2013). Coastal wave field extraction using TerraSAR-X data. *Journal of Applied Remote Sensing*, *7*, 20. <https://doi.org/10.1117/1.JRS.7.073.694>
- Cavaleri, L. (2000). The oceanographic tower Acqua Alta—Activity and prediction of sea states at Venice. *Coastal Engineering*, *39*, 29–70.
- Collins, C., & Rogers, W. E. (2017). A source term for wave attenuation by sea ice in WAVEWATCH III[®]: IC4 (NRL Report NRL/MR/7320–17-9726) (25 pp.). Washington, DC: NRL. (Retrieved from <https://www7320.nrlssc.navy.mil/pubs.php>)

Acknowledgments

We thank Birgit Schaettler (DLR) and Egbert Schwarz (DLR) for their support with the TerraSAR-X data acquisition and Adam Inch (UVic) for his help in providing the science crew on R/V Sikuliaq with remote sensing products. Discussions with Andrey Pleskachevsky (DLR) helped to optimize the TerraSAR-X wave height retrieval algorithm used in this project. Li Li (NRL) processed the AMSR2 ice concentration data used herein. Reviews by Luigi Cavaleri and an anonymous reviewer helped to improve the manuscript. Funding for this project came from the U.S. Office of Naval Research DRISea State and Boundary Layer Physics in the Emerging Arctic with awards: N00014-13-1-0280 (J. G.), N0001414WX20022 (E. R.), N00014-13-1-0284 (J. T.), and N00014-13-1-0xxx (S. L.). TerraSAR-X data were provided by DLR under AO OCE1837 (J. G.). Data are accessible via <http://www.apl.uw.edu/arcticseastate>.

- Comiso, J. C., Cavalieri, D. J., & Markus, T. (2003). Sea ice concentration, ice temperature, and snow depth using AMSR-E data. *IEEE Transactions on Geoscience and Remote Sensing*, *41*(2), 243–252.
- Gebhardt, C., Bidlot, J. R., Jacobsen, S., Lehner, S., Persson, P. O. G., & Pleskachevsky, A. L. (2017). The potential of TerraSAR-X to observe wind wave interaction at the ice edge. *IEEE Journal of Selected Topics in Applied Earth Observations and Remote Sensing*, *10*(6), 2799–2809. <https://doi.org/10.1109/JSTARS.2017.2652124>
- Gemrich, J., Pleskachevsky, A., Lehner, S., & Rogers, E. (2015). Surface waves in arctic seas, observed from TerraSAR-X. In *2015 IEEE International Geoscience and Remote Sensing Symposium (IGARSS)*, Milan, Italy. <https://doi.org/10.1109/IGARSS.2015.7326604>
- Gemrich, J., Thomson, J., Rogers, W. E., Pleskachevsky, A., & Lehner, S. (2016). Spatial characteristics of ocean surface waves. *Ocean Dynamics*, *66*, 1025–1035.
- Hasselmann, K., Barnett, T., Bouws, E., Carlson, H., Cartwright, D., Enke, K., et al. (1973). Measurements of wind-wave growth and swell decay during the Joint North Sea Wave Project (JONSWAP). *Deutsche Hydrographische Zeitschrift, Ergänzungsheft Reihe A*, *12*(8), 1–95.
- Hogan, T., Liu, M., Ridout, J. A., Peng, M. S., Whitcomb, T. R., Ruston, B. C., et al. (2014). The Navy Global Environmental Model. *Oceanography*, *27*(3), 116–125.
- Holthuijsen, L. H. (2007). *Waves in oceanic and coastal waters*. U. K.: Cambridge University Press. 387 pp.
- Kahma, K., & Calkoen, C. (1992). Reconciling discrepancies in the observed growth of wind-generated waves. *Journal of Physical Oceanography*, *22*, 1389–1405.
- Metzger, E., Helber, R., Hogan, P., Throppil, P., Posey, P. G., Townsend, T., et al. (2017). Global Ocean Forecast System 3.1 validation testing. Tech. rep (Report NRL/MR/7320–17-9722). Washington, DC: NRL.
- Pleskachevsky, A., Rosenthal, W., & Lehner, S. (2016). Meteo-marine parameters for highly variable environment in coastal regions from satellite radar images. *ISPRS Journal of Photogrammetry and Remote Sensing*, *119*, 464–484.
- Posey, P., Metzger, E. J., Wallcraft, A. J., Hebert, D., Allard, R., Smedstad, O., et al. (2015). Improving Arctic sea ice edge forecasts by assimilating high horizontal resolution sea ice concentration data into the US Navy's ice forecast systems. *The Cryosphere*, *9*, 1735–1745.
- Ren, Y., Lehner, S., Bruschi, S., Li, X., & He, M. (2012). An algorithm for the retrieval of sea surface wind fields using X-band TerraSAR-X data. *International Journal of Remote Sensing*, *33*, 7310–7336.
- Rogers, W. E., Posey, P., Li, L., & Allard, R. A. (2018). Forecasting and hindcasting waves in and near the marginal ice zone: Wave modeling and the ONR “Sea State” field experiment (NRL Memorandum Report NRL/MR/7320–18-9786): NRL. 179 pp. [available from <https://www7320.nrlssc.navy.mil/pubs.php>].
- Rogers, W. E., Thomson, J., Shen, H. H., Doble, M. J., Wadhams, P., & Cheng, S. (2016). Dissipation of wind waves by pancake and frazil ice in the autumn Beaufort Sea. *Journal of Geophysical Research*, *121*, 7991–8007. <https://doi.org/10.1002/2016JC012251>
- Rikka, S., Pleskachevsky, A., Uiboupin, R., & Jacobsen, S. (2018). Sea state in the Baltic Sea from space-borne high-resolution synthetic aperture radar imagery. *International Journal of Remote Sensing*, *39*, 1256–1284. <https://doi.org/10.1080/01431161.2017.1399475>
- Smith, M., Stammerjohn, S., Persson, O., Rainville, L., Liu, G., Perrie, W., et al. (2018). Episodic reversal of autumn ice advance caused by release of ocean heat in the Beaufort Sea. *Journal of Geophysical Research: Oceans*, *123*, 3164–3185. <https://doi.org/10.1002/2018JC013764>
- Smith, M., & Thomson, J. (2016). Scaling observations of surface waves in the Beaufort Sea. *Elementa*, *4*, 97. <https://doi.org/10.12952/journal.elementa.000097>
- The WAVEWATCH III Development Group (WW3DG) (2016). User manual and system documentation of WAVEWATCH III version 5.16 (Tech. Note, 329). College Park, MD, USA: NOAA/NWS/NCEP/MMAB. 326 pp. + Appendices.
- Thomson, J. (2012). Wave breaking dissipation observed with SWIFT drifters. *Journal of Atmospheric and Oceanic Technology*, *29*, 1866–1882.
- Thomson, J., Ackley, S., Girard-Ardhuin, F., Ardhuin, F., Babanin, A., Boutin, G., et al. (2018). Overview of the Arctic Sea State and Boundary Layer Physics Program. *Journal of Geophysical Research: Oceans*, *123*. <https://doi.org/10.1002/2018JC013766>
- Thomson, J., Fan, Y., Stammerjohn, S., Stopa, J., Rogers, W. E., Girard-Ardhuin, F., et al. (2016). Emerging trends in the sea state of the Beaufort and Chukchi Seas. *Ocean Modelling*, *105*, 1–12. <https://doi.org/10.1016/j.ocemod.2016.02.009>
- Thomson, J., & Rogers, W. E. (2014). Swell and sea in the emerging Arctic Ocean. *Geophysical Research Letters*, *41*, 3136–3140. <https://doi.org/10.1002/2014GL059983>
- Tolman, H. (2002). Validation of WAVEWATCH III version 1.15 for a global domain (Tech. Rep. 213, NCEP Technical Note). Silver Hill Road, Washington, DC: NOAA/NWS/NCEP/OMB.
- Wang, X. L., Feng, Y., Swail, V. R., & Cox, A. (2015). Historical changes in the Beaufort–Chukchi–Bering Seas surface winds and waves, 1971–2013. *Journal of Climate*, *28*(19), 7457–7469. <https://doi.org/10.1175/JCLI-D-15-0190.1>
- Zippel, S., & Thomson, J. (2016). Air-sea interactions in the marginal ice zone. *Elementa*, *4*, 95. <https://doi.org/10.12952/journal.elementa.000095>